

Article

Spectrophotometric Characterization of Thin Semi-Transparent Aluminum Films Prepared by Electron Beam Evaporation and Magnetron Sputtering

Steffen Wilbrandt ^{1,*}, Olaf Stenzel ^{1,2}, Abrar Liaf ^{1,2}, Peter Munzert ¹, Stefan Schwinde ¹, Sven Stempfhuber ¹, Nadja Felde ¹, Marcus Trost ¹, Tina Seifert ¹ and Sven Schröder ¹

¹ Fraunhofer Institute of Applied Optics and Precision Engineering IOF, Albert-Einstein Str. 7, 07745 Jena, Germany

² Abbe School of Photonics, Friedrich-Schiller-University Jena, Albert-Einstein-Str. 6, 07745 Jena, Germany

* Correspondence: steffen.wilbrandt@iof.fraunhofer.de

Abstract: Aluminum thin films with thicknesses between approximately 10 and 60 nm have been deposited by evaporation and sputtering techniques. Layer characterization focused on reflectance, optical constants, and surface quality. Reflectance fits have been performed using a merger of three standard dispersion models, namely the Drude model, the Lorentzian oscillator model, and the beta-distributed oscillator model. A thickness dependence of the optical constants could be established in the investigated thickness range.

Keywords: aluminum films; film thickness; layer deposition; optical constants; reflectance



Citation: Wilbrandt, S.; Stenzel, O.; Liaf, A.; Munzert, P.; Schwinde, S.; Stempfhuber, S.; Felde, N.; Trost, M.; Seifert, T.; Schröder, S.

Spectrophotometric Characterization of Thin Semi-Transparent Aluminum Films Prepared by Electron Beam Evaporation and Magnetron Sputtering. *Coatings* **2022**, *12*, 1278. <https://doi.org/10.3390/coatings12091278>

Academic Editor: Joaquim Carneiro

Received: 11 July 2022

Accepted: 28 August 2022

Published: 1 September 2022

Publisher's Note: MDPI stays neutral with regard to jurisdictional claims in published maps and institutional affiliations.



Copyright: © 2022 by the authors. Licensee MDPI, Basel, Switzerland. This article is an open access article distributed under the terms and conditions of the Creative Commons Attribution (CC BY) license (<https://creativecommons.org/licenses/by/4.0/>).

1. Introduction

Aluminum is one of the basic optical materials used today and finds applications from the infrared to the vacuum ultraviolet (VUV) spectral regions, preferable as a reflector material. Particularly in the VUV, properly protected high quality aluminum films are basic constituents of state-of-the-art reflector elements [1–3]. However, in the visible spectral range (VIS), rather thick aluminum films are used in high-end optical systems such as cameras, telescopes, projectors, smart back reflectors for vehicles or the like [4].

Aluminum films are conveniently produced by evaporation and sputtering techniques [5,6]. According to the »quick and cold« rule, high quality aluminum films are usually manufactured with large deposition rates and without substrate heating. The optical properties of rather thick aluminum films are well understood, and optical constants are tabulated in different studies [7–9]. Moreover, the influence of thin seed layers (e.g., Cu, CuO_x, Cr, CrO_x, Au, or Ag) on the morphology and the reflectance of aluminum layers prepared by sputtering and e-beam evaporation are well-known [10,11]. Because of their importance in precision optics, bulk aluminum reference data may also be found in the databases of relevant software packages (see for example [12]).

Besides applications as a reflector coating, there are situations where the transmissive properties of aluminum layers may be of interest. Generally, any sufficiently thick metal (not necessary aluminum) film has application potential as a reflector coating in broad spectral regions. But if the film thickness becomes significantly smaller than approximately 100 nm, the metal films become semitransparent. In this thickness range they may find application in different kinds of metal-dielectric interference coatings, including for example bandpass filters [13] or architectural coatings [4]. Other applications of ultrathin metal films may concern different branches of optoelectronics, as well as black coatings or plasmonic devices. Therefore, ultrathin (but closed) metal films have attracted an increasing attention in the optical coating's community in the last years [14–17].

However, data on the optical properties of semi-transparent metal (and in particular aluminum) films are rare. This might be due to a specific complication, namely the thickness-dependence of the optical constants of metal films in the thickness range of a few nanometer [16,17]. This thickness dependence prevents both design and characterization of coatings with ultrathin metal films from being a routine task [14].

Besides applications scenarios in thin film multilayer coatings, modelling of ultrathin aluminum film spectra is of use for in situ optical monitoring of the early stages of aluminum film growth [18,19]. In an ex situ spectrophotometric study of Du et al. [20], a thickness dependence of the aluminum film optical constants could clearly be confirmed in the thickness range up to approximately 30 nm. In a more recent study [21], we have investigated the thickness dependence of the optical constants of copper and gold ultrathin films in terms of a model that explicitly considers mean free path effects (see later Section 2.2). The changes in the optical constants with thickness are significant, and therefore, thickness-dependent optical constants must be taken into account in any relevant design calculation.

Let us also mention that the thickness dependence investigated here is restricted to closed metal films, i.e., it is not due to a change with growth morphology of a metal island film [17,22–25]. In the present study, we will therefore assume that the films are thick enough such that they can be assumed as closed films, and not as a sort of island films. This clearly restricts the relevant thickness range from below, such that we restrict on films with a minimum thickness close to 10 nm. The maximum thickness is given by the requirement of certain transparency.

Therefore, in order to address potential applications in transmissive optics, the purpose of the present study is to establish and compare the optical constants of aluminum films in the thickness range between approximately 10 and 60 nm. The analysis will be performed in the wavelength range 200–2500 nm and thus includes parts of the near infrared (NIR), the visible (VIS) and parts of the ultraviolet (UV) spectral range. The focus is on a systematic investigation of the thickness-dependence of the Drude damping parameter in ultrathin aluminum films, which defines the primary novelty of this paper.

2. Theory

2.1. Dispersion Parameters

As it turns out from characterization studies such as [7,26], a convenient description of the aluminum optical constants is possible in terms of parametrized dispersion models, which consider the free electron response in terms of the classical Drude function, and the bound electrons in terms of an oscillator model [27,28]. In the spectral range considered in the present study, both free and bound electrons contribute to the optical response of the metal in a specific manner. The idea of our approach is to consider the contribution of free electrons (as usual) in terms of the Drude function. The resonant response of interband transitions located far in the VUV (larger than 7.9 eV photon energy—compare [7]) is outside our measurement range, and we condense the non-resonant effect of all these transitions into one Lorentzian oscillator located in the VUV. The critical point interband transitions that give rise to the prominent aluminum spectral feature around the wavelength of 830 nm (W_1 – W_2' , W_1 – W_3' and Σ_1 – Σ_3 gaps in the assignment of Ehrenreich [7]) fall into our measurement range. Because of the complex origin and spectral structure, this absorption feature will be modelled in terms of the β_{do} model [29,30].

Figure 1 visualizes reference data on the optical constants of aluminum as selected from different sources in the spectral range relevant for our study. Obviously, bulk optical constants of aluminum show only marginal discrepancies among different sources.

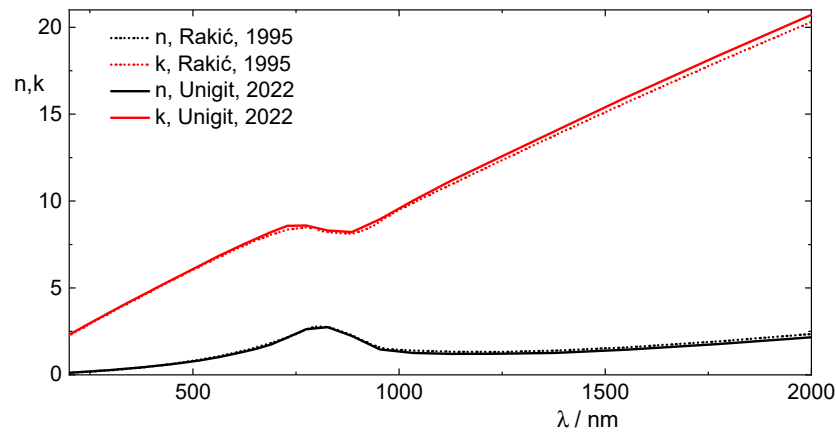


Figure 1. Reference data on the optical constants of aluminum (bulk or non-transparent films) [9,12].

In order to account for both the free and bound electrons fractions in a metal film, we make use in Equation (1) of the following writing of the metal’s dielectric function ϵ (n —refractive index; k —extinction coefficient) (all formulas in this paragraph stemming from references [21,31]):

$$\epsilon = 1 + \chi_{\text{free}} + \underbrace{\chi_{\text{bound}}}_{=\chi_{\text{Lor}}+\chi_{\beta}} = (n + ik)^2 \tag{1}$$

Here, we use symbols as introduced in our previous study [21], such that χ_{free} is the susceptibility characterizing the free electrons, and χ_{bound} describes the bound electrons. The later sums up from one Lorentzian oscillator (Equation (2) [27,28]):

$$\chi_{\text{Lor}} = \frac{J_0}{\pi} \left(\frac{1}{\nu_0 - \nu - i\Gamma_0} + \frac{1}{\nu_0 + \nu + i\Gamma_0} \right) \tag{2}$$

and one beta distributed oscillator (β_{do}) in Equation (3) [28,29]:

$$\chi_{\beta} = \frac{I}{\pi} \int_{\nu_a}^{\nu_b} w_{\beta}(\xi) \left[\frac{1}{\xi - \nu - i\Gamma} + \frac{1}{\xi + \nu + i\Gamma} \right] d\xi$$

$$d\xi w_{\beta}(\nu) = \begin{cases} \frac{(\nu - \nu_a)^{A-1} (\nu_b - \nu)^{B-1}}{\int_{\nu_a}^{\nu_b} (\nu - \nu_a)^{A-1} (\nu_b - \nu)^{B-1} d\nu}; & A, B > 0; \nu \in (\nu_a, \nu_b) \\ 0; & \nu \notin (\nu_a, \nu_b) \end{cases} \tag{3}$$

$$\Delta\nu = \nu_b - \nu_a$$

For the free electrons, we will use the classical Drude function (Equation (4)) [27,31]:

$$\chi_{\text{free}} = - \left(\frac{\nu_p^2}{\nu^2 + 2i\nu\Gamma_D} \right) \tag{4}$$

Here ν is the wavenumber (e.g., the reciprocal value of the vacuum wavelength), and ν_p the free electrons plasma frequency in wavenumber units. For the bulk material, we have the Drude damping parameter (Equation (5)):

$$\Gamma_{D,b} = \frac{1}{4\pi c\tau_b} \tag{5}$$

with the bulk collision time τ_b . Particularly, for the “perfect” bulk crystal, Equation (5) reads as:

$$\Gamma_{D,b0} = \frac{1}{4\pi c\tau_{b0}} \tag{6}$$

According to [32], the theoretical value on the bulk collision time τ_{b0} in the perfect crystal is $\tau_{b0} = 11.8$ fs, which corresponds to a value $\Gamma_{D,b0} = 225 \text{ cm}^{-1}$ in Equation (6).

Different sets of Drude parameters (Table 1) are obtained or used in studies published in the past decades. The reported data scatter strongly but are of the same order of magnitude.

Table 1. Survey of literature data on aluminum Drude parameters. Numerical values have been adopted to the writing of the Drude function given in Equation (4).

Reference	ν_p/cm^{-1}	Γ_D/cm^{-1}
[7]	102,400	518
[26]	119,000	330
[33]	120,800	165
[34]	97,100	519

Similarly, to the spread of data as observed in gold and copper [21], the relative spread in reported Γ_D values is considerably larger than in the case of the plasma frequency. We see possible reasons in differences in the sample quality as well as different model approaches when determining the optical constants.

2.2. Mean Free Path Effects

As successfully demonstrated in [21], the Anderson approach [35,36] may be used to model the thickness dependence of the Drude parameter in ultrathin metal coatings in terms of the mean free path model. Then:

$$\tau(d) = \frac{\tau_b}{\left[1 + 2 \frac{(1-p_{\text{spec}})l_{\text{free}}}{d}\right]} \quad (7)$$

In Equation (7), p_{spec} is the relative amount of charge carriers that is specularly reflected at the film surface, and l_{free} the mean free path in the bulk material. Note that in this approach, only charge carriers that reflected diffusely from the surface contribute to the mentioned thickness dependence. When setting $l_{\text{free}} = v_F \tau_b$ with v_F being the Fermi velocity and making use of Equation (6), we obtain a manageable expression for the thickness-dependent Drude damping parameters in thin films according to:

$$\Gamma_D(d) = \Gamma_{D,b} \left[1 + \frac{2(1-p_{\text{spec}})v_F \tau_b}{d}\right] \quad (8)$$

This expression (Equation (8)) will be the basis of our discussion of thickness-dependent Drude parameters in ultrathin aluminum films. It clearly predicts a significant increase in the Drude damping parameter when the film thickness becomes smaller than twice the mean free path of the free electrons. The physical reason is in the growing amount of surface collision events compared to bulk collision events. Note that according to [32], in perfect aluminum we have $v_F \tau_{b0} = 18.9$ nm. In real aluminum films, the mean free path is expected to be smaller than this value.

3. Experimental

3.1. Layer Deposition

To get access to possible dependencies of the optical constants on the deposition techniques, three sample series have been produced by magnetron sputtering and electron beam evaporation in two different experimental setups. The main deposition parameters are provided in the following sections.

3.1.1. Series 1: Magnetron Sputtering

The depositions were performed with an inline magnetron sputtering system (MRC from Kenotec SRL, Italy) with a top-down arrangement. The target geometry of this system is 120 mm × 380 mm. The distance between the aluminum target and the substrates is about 60 mm. During the process, the substrates scan vertical to the narrow side of the target. The layer thickness is controlled by determining the deposition rate in a preliminary test (by X-ray reflectometry with a Bruker D8) and adjusting the number of scans and scan velocity. The scan velocity was 117 cm/min. Taking the dynamic deposition rate (calculated by multiplying the measured film thickness with the transportation speed) into account, 10 nm of aluminum has been deposited per scan. For the deposition of the different aluminum thicknesses, the number of scans has varied between 1 and 5.

Fused silica Q1 substrates mounted onto a grounded substrate holder have been used in series 1. Before the aluminum deposition, the substrates were cleaned using a high-frequency etching station to remove H₂O and carbon residues from the surface. Subsequently, the aluminum was deposited by DC-sputtering using a pure aluminum target (purity level 5N ≅ 99.999%) and Ar as the sputtering gas. Detailed parameters that were used for manufacturing of the aluminum layers are summarized in Table 2.

Table 2. Process sequence and parameters for aluminum deposition series 1.

Process Sequence		Parameters for Series 1
Vacuum Pumping	Base Pressure	$<5 \times 10^{-6}$ mbar
Plasma pre-treatment	duration	~60 s
	power	100 W
	gas flow Ar	35 sccm
	gas flow O ₂	0 sccm
Aluminum deposition	process pressure	$\sim 1.5 \times 10^{-6}$ mbar
	power	500 W
	gas flow Ar	10 sccm
	dynamic deposition rate	11.7 nm m/min

3.1.2. Series 2 and 3: Electron Beam Evaporation

The aluminum layers have been deposited in Bühler Syrus pro 1110 coating machines by e-beam evaporation from a molybdenum liner. As evaporation material, aluminum rods (purity 99.98%) from Umicore were used. Fused silica Q1 substrates have been used in series 2, and fused silica Mabuchi substrates for series 3. Substrate pre-conditioning was performed by plasma etching using the APS plasma source, which is part of the evaporation plant. The evaporation rate and the thickness termination were controlled by quartz crystal monitoring.

Note that in series 3, additional plasma assistance by the Bühler APS pro plasma source was supplied. We do not expect superb layer properties with regard to reflector applications from that, but the comparison between assisted and unassisted samples will be interesting anyway, maybe for identifying alternative application fields.

Thickness calibration has been performed by X-ray reflectometry (XRR) with a Bruker D8. Detailed deposition parameters, which were used for manufacturing of the aluminum layers, are summarized in Table 3.

Table 3. Process sequence and parameters for aluminum deposition series 2 and 3.

Process Sequence		Parameters for Series 2	Parameters for Series 3
Vacuum Pumping	Base Pressure	$<5 \times 10^{-6}$ mbar	
Plasma pre-treatment	duration		180 s
	APS BIAS Voltage	125 V	140 V
	gas flow Ar		12 sccm
	gas flow O ₂	0 sccm	0–10 sccm

Table 3. Cont.

Process Sequence		Parameters for Series 2	Parameters for Series 3
Aluminum deposition	deposition rate	2–3 nm/s	~0.1 nm/s
	substrate temperature	room temperature	120 °C
	APS Bias Voltage	0	120 V
	gas flow Ar	0 sccm	12 sccm
	gas flow O ₂	0 sccm	0 sccm

3.2. Layer Characterization

3.2.1. Spectrophotometry

T- and R-spectra in the range of 200–2500 nm of all samples have been measured ex situ at near normal incidence in a Perkin Elmer Lambda 950 scanning spectrophotometer equipped with absolute T and R measurement attachments. Note that reflectance spectra have been recorded with light incident from both film and substrate sides. From these spectra, the optical constants *n* and *k* have been deduced from spectra fits using a Matlab environment. Thereby, film thickness data as obtained from XRR or an optical sum-rule treatment (see later Section 4.1) have been assumed as fixed parameters.

In order to account for the ultrathin native aluminum oxide layer that is formed on the aluminum film immediately after its exposure to air, we have applied a two-layer model (Figure 2), comprising the aluminum film under investigation with an ultrathin alumina layer on top. Because of a lack of corresponding data, the optical constants of the ultrathin native oxide layers have been taken from stoichiometric aluminum oxide films from the institute’s internal database.

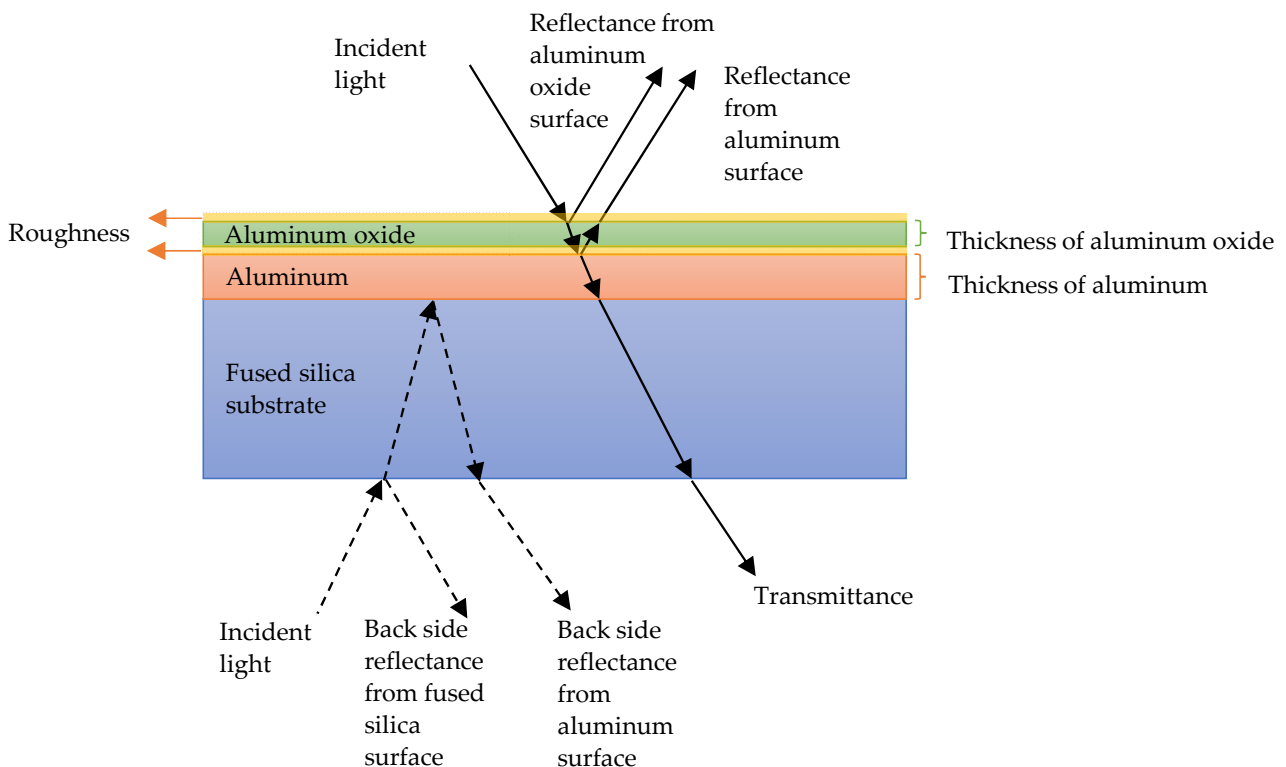


Figure 2. Layer model. Yellow regions denote interface roughness and arrows indicate beam propagation.

3.2.2. X-ray Reflection (XRR)

The specular X-ray reflection is used to determine the thickness, density, and surface roughness of the thin aluminum layers. For this purpose, the X-ray diffractometer D8 Discover from Bruker AXS in Bragg-Brentano geometry was used. This diffractometer

has a copper X-ray tube and uses the characteristic K_{α} radiation with a wavelength of $\lambda = 0.154$ nm. In the course of this work, all measurements were performed with an acceleration voltage of 40 kV and a cathode current of 40 mA. The relative wavelength error $\Delta\lambda_{K_{\alpha}}/\lambda_{K_{\alpha}}$ is approx. 0.1% while the absolute angle error $\Delta\theta$ is 0.002° .

In this method, intensity measurements are carried out at different angles of incidence. Since the phase information of the reflected radiation is lost during the intensity measurement, no inverse Fourier transforms can be used to draw conclusions about the nature of the sample. Instead, simulations of assumed layers have to be calculated and adapted to the measured curves. The applied layer model consists of the fused silica substrate, an aluminum layer, and the native formed aluminum oxide layer as shown in Figure 2. The commercially available Leptos 7 software from Bruker AXS was used to fit the simulated XRR data to the measured curves. The results for the layer thicknesses, surface roughness, and layer densities are summarized later in Table 4.

Table 4. Results of XRR investigations.

Deposition Method	Al	Al _x O _y	Al	Al _x O _y	Al	Al _x O _y
	d/nm		σ/nm		ρ/(g·cm ⁻³)	
Sputtering Series 1	8.3	3.1	1.1	1.3	2.6989	3.9836
	18.0	2.1	1.4	2.3		
	29.7	1.0	1.2	1.8		
	39.9	1.4	1.0	1.9		
	49.1	1.5	1.2	2.3		
Evaporation Series 2	8.0	1.9	1.0	1.4	2.6989	3.9836
	16.3	1.2	2.1	1.5		
	22.4	1.2	2.0	1.5		
	29.7	1.0	1.6	1.6		
	37.5	1.1	2.0	1.6		
Assisted Evaporation Series 3	18		2.8		2.85	-
	38	-	3.8	-		
	40		3.3			
	62		7.0			

3.2.3. Atomic Force Microscopy (AFM)

Roughness characterization of the samples was performed using an atomic force microscope Dimension Icon from Bruker, operating in tapping mode. Scan areas of $1 \mu\text{m} \times 1 \mu\text{m}$, $10 \mu\text{m} \times 10 \mu\text{m}$, and $50 \mu\text{m} \times 50 \mu\text{m}$ each containing 512×512 data points, were analyzed with single crystalline Si probes (5 nm nominal tip radius), which covers the high spatial frequency range ($f > 1 \mu\text{m}^{-1}$). The surface topography data were used to determine the rms-roughness and roughness spectra. The rms-roughness is defined as the standard deviation of a surface profile, $h(x, y)$ [37,38]

$$\sigma = \left\{ \frac{1}{L_x L_y} \int_{-\frac{L_y}{2}}^{\frac{L_y}{2}} \int_{-\frac{L_x}{2}}^{\frac{L_x}{2}} [h(x, y) - \bar{h}]^2 dx dy \right\}^{\frac{1}{2}} \quad (9)$$

with the scan length L_x and L_y of the profile and the mean surface height \bar{h} . The rms roughness only describes vertical differences in the surface topography. In order to include the lateral characteristics, the power spectral density functions (PSDs) would have to be determined, which represent the relative strength of each roughness component within a surface area L , as a function of spatial frequencies (f_x, f_y) [39]:

$$PSD(f_x, f_y) = \lim_{L \rightarrow \infty} \frac{1}{L^2} |FT[h(x, y)]|^2 \quad (10)$$

Here, FT denotes a Fourier transformation. The PSDs of different measurement areas may be combined to a unique PSD function to discuss the roughness evolution [40] of the thin films over a wide spatial frequency range.

3.2.4. Scanning Electron Microscopy (SEM)

The layer surfaces were investigated using a Carl Zeiss Sigma scanning electron microscope (Jena, Germany). The applied acceleration voltage was 5 kV and an InLens-Detector was used to detect the secondary electrons. To get a good overview, images were made in different magnifications. The presented results were made with a magnification of 70,000.

4. Results

4.1. Non-Optical Properties

4.1.1. Film thickness

In order to determine the metal film thickness, three different approaches have found application:

- i Quartz crystal monitoring data during deposition (electron beam evaporation only);
- ii X-ray reflection (XRR) analysis;
- iii From measured T- and R-spectra without assuming a specific dispersion law, but on the basis of a sum-rule based theoretical approach [19,41].

Figure 3 presents results of thickness determination from methods ii and iii for magnetron sputtered samples with given target thickness. Obviously, the data are well consistent. In the following, we always use the thicknesses as determined by XRR (see Table 4).

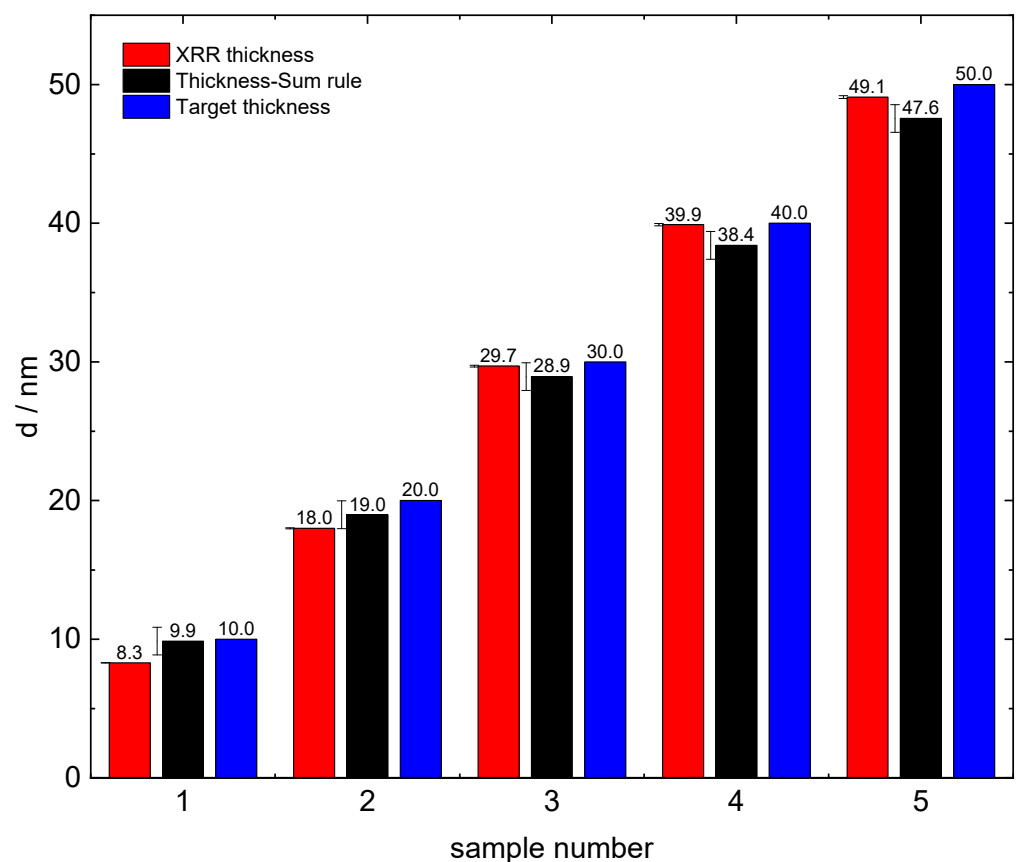


Figure 3. Geometrical thicknesses of aluminum layers prepared by sputtering (series 1). Sample numbers corresponding to the order of samples in Table 4.

Table 4 also provides data on the thickness of the native alumina overlayer as well as the rms surface roughness visualized in Figure 2 in yellow. The alumina layer thickness as obtained by XRR has been used later as a fixed input parameter for the fits of T and R of the samples. The extraordinarily large aluminum roughness as obtained from the series 3 layers prevented us from reliable determination of parameters of the alumina overlayer, so these data are absent in the table. In the spectra fits shown later, the alumina overlayer thickness has been set to be 1.6 nm. Note that the density of the assisted layers turned out to be increased compared to the Series 1 and 2 layers.

4.1.2. Surface Topology

SEM: In order to illustrate the rather large roughness values as obtained from series 3 layers, Figure 4 illustrates the surface topology obtained by SEM of a 62 nm and a 40 nm thick aluminum film from series 3. Note the complicated surface topology, probably caused here by the low deposition rate used in series 3. SEM images of samples from series 2 were almost structureless, an effect that we assign to the completely different deposition conditions. Therefore, additional AFM measurements have been performed for quantitative investigation of the surface profiles relevant for series 1 and 2.

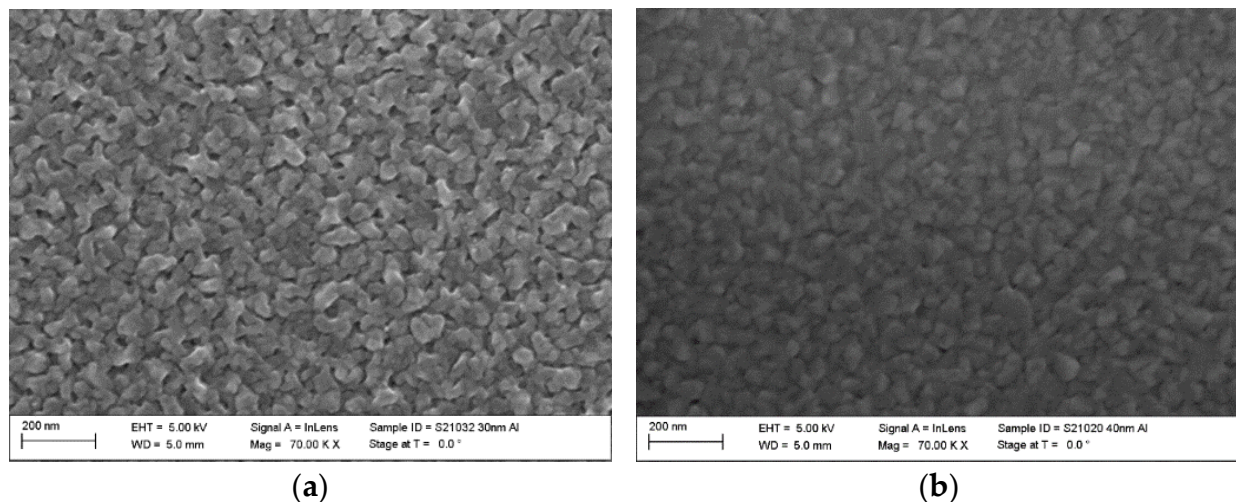


Figure 4. SEM image of a 62 nm (a) and 40 nm (b) thick aluminum film on fused silica glass prepared by electron beam evaporation with plasma assistance (series 3). The bad quality of the SEM image of the thinner sample is due to the electric charging of the sample, caused by the insulating substrate and the lower film thickness.

AFM: AFM topography measurements have only been performed on the samples deposited on fused silica, i.e., from series 1 and 2. In Figure 5, AFM images are shown for two layer thicknesses. In Figure 6, the rms roughness values obtained from the $1 \mu\text{m} \times 1 \mu\text{m}$ AFM scans (black triangles) based on the surface height data and Equation (9) are compared to the Al_xO_y roughness as obtained from XRR (red triangles). All in all, the XRR and AFM roughness data are close to each other. The surface roughness values obtained from the fit of spectrophotometric data (blue triangles) are also shown; these roughness data are generally significantly larger than those obtained from AFM and XRR. The obvious reason is in specifics of the optical model applied for spectra fitting, as it will be discussed later in the discussion section.

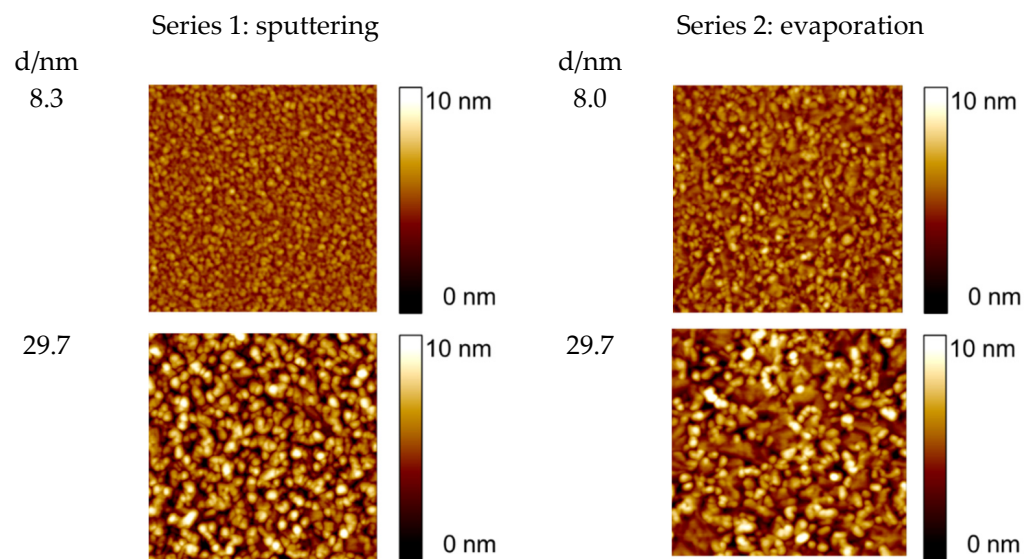


Figure 5. Selected AFM images of the metal films surface morphology. The mentioned thicknesses correspond to those obtained from XRR.

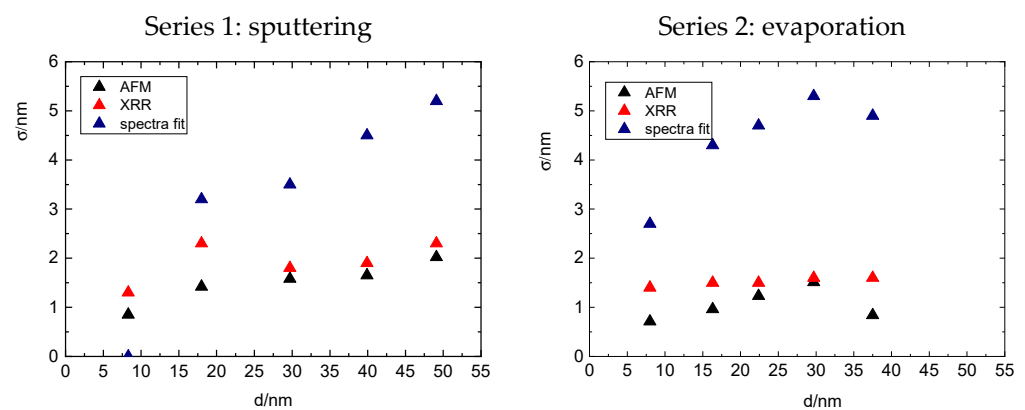


Figure 6. Rms roughness σ of the alumina overlayer vs. aluminum thickness d as obtained from XRR.

4.2. Optical Properties

Concerning the optical properties, let us first mention that all spectra of series 1 and 2 samples could be well fitted by means of the chosen dispersion approach. Thus, a total of 11 independent dispersion parameters (2 Drude parameters for the response of free electrons Equation (4), 6 β_{do} parameters for the characteristic NIR spectral feature caused by bound electron absorption Equation (3), and 3 Lorentzian oscillator parameters for the non-resonant contributions of bound electron resonances in the VUV Equation (2)) were necessary to model the optical constants of the aluminum film in each of the samples.

Note that all film thicknesses have been set equal to those obtained by XRR, hence the thicknesses have not been used as fitting parameters. Moreover, the optical constants of the Al_xO_y layer have been kept at fixed values, corresponding to stoichiometric Al_2O_3 . However, a large-scale roughness of the first surface (Al_xO_y —air) has been considered as a further fitting parameter [42].

The fit quality is exemplified in Figure 7. BR denotes the reflectance measured for light incident from the substrate side.

All fitting parameters are summarized in Tables 5–7. The value ν_0 will anyway be outside our accessible spectral range, it was therefore fixed at $65,000 \text{ cm}^{-1}$ in all fits.

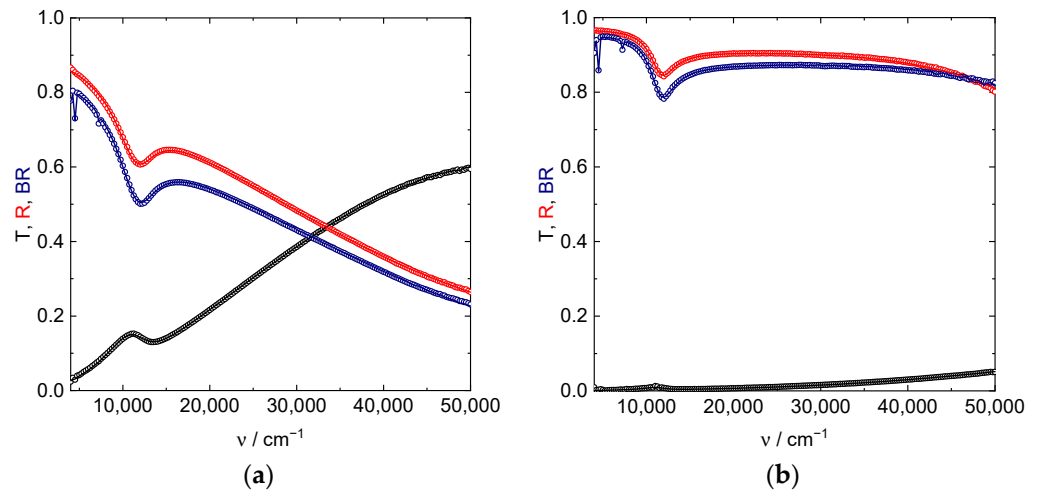


Figure 7. Fit examples for samples from series 2: experimental spectra (triangles) and fit (lines). (a) $d = 8.0 \text{ nm}$; (b) $d = 29.7 \text{ nm}$. The samples are identical to the evaporated samples shown in Figure 5.

Table 5. Dispersion parameters of series 1 films (sputtering).

Dispersion Model Contribution:	$d_{Al,XRR}/\text{nm}$	8.3	18.0	29.7	39.9	49.1
Drude Equation (4)	ν_p/cm^{-1}	110,124	108,923	105,132	106,123	123,834
	Γ_D/cm^{-1}	1064.4	901.3	823.9	791.5	927.1
β_do Equation (3)	ν_a/cm^{-1}	12,066	11,870	11,564	11,565	11,292
	$\Delta\nu/\text{cm}^{-1}$	131,106	202,425	443,938	461,171	919,485
	J/cm^{-1}	305,720	296,174	276,788	290,959	455,017
	Γ/cm^{-1}	2712.5	2003.6	1727.6	1687.7	1579.9
	A	0.000	0.082	0.001	0.000	0.000
Lorentzian Equation (2)	B	7.766	14.472	27.948	28.904	65.992
	ν_0/cm^{-1}	65,000	65,000	65,000	65,000	65,000
	J_0/cm^{-1}	68,088	39,644	27,219	29,447	130,803
	Γ_0/cm^{-1}	31,039	18,509	11,909	7800	90
	σ_{Al}/nm	0.0	0.0	0.0	0.0	0.0
	$\sigma_{Al_2O_3}/\text{nm}$	2.7	0.0	3.2	3.5	4.5
	$d_{Al_2O_3}/\text{nm}$	1.9	3.1	2.1	1.0	1.4

Table 6. Dispersion parameters of series 2 films (evaporation).

Dispersion Model Contribution:	$d_{Al,XRR}/\text{nm}$	8.0	16.3	22.4	29.7	37.5
Drude Equation (4)	ν_p/cm^{-1}	107,397	103,963	105,581	106,440	108,328
	Γ_D/cm^{-1}	963.4	822.3	781.2	767.5	811.8
β_do Equation (3)	ν_a/cm^{-1}	12,165	12,055	11,982	11,941	11,881
	$\Delta\nu/\text{cm}^{-1}$	37,246	43,681	49,097	62,348	93,918
	J/cm^{-1}	283,115	263,706	274,932	284,404	293,826
	Γ/cm^{-1}	2446.7	1811.7	1638.2	1546.6	1480.1
	A	0.122	0.176	0.199	0.214	0.225
Lorentzian Equation (2)	B	3.350	3.879	4.454	5.652	8.727
	ν_0/cm^{-1}	65,000	65,000	65,000	65,000	65,000
	J_0/cm^{-1}	117,565	234,658	143,772	230,593	1,057,703
	Γ_0/cm^{-1}	44,812	112,896	88,830	125,819	259,820
	σ_{Al}/nm	0.0	0.0	0.0	0.0	0.0
	$\sigma_{Al_2O_3}/\text{nm}$	2.7	4.3	4.7	5.3	4.9
	$d_{Al_2O_3}/\text{nm}$	1.9	1.2	1.2	1.0	1.1

Table 7. Dispersion parameters of series 3 films (assisted evaporation).

Dispersion Model Contribution:	$d_{Al,XRR}/nm$	18.0	38.0	40.0	62.0
Drude Equation (4)	ν_p/cm^{-1}	48,902	65,374	101,313	64,280
	Γ_D/cm^{-1}	8914.9	815.8	932.3	831.1
β_do Equation (3)	ν_a/cm^{-1}	2224	10,360	11,932	11,336
	$\Delta\nu/cm^{-1}$	18,127	1,032,317	148,323	58,417
	J/cm^{-1}	841,157	262,484	283,329	115,795
	Γ/cm^{-1}	6826.0	3860.7	2465.8	1675.6
	A	0.000	0.044	0.010	0.316
	B	0.091	57.076	7.880	1.790
Lorentzian Equation (2)	ν_0/cm^{-1}	65,000	65,000	65,000	65,000
	J_0/cm^{-1}	127,847	43,810	214,250	3262
	Γ_0/cm^{-1}	45,019	32,507	78,407	1,295,243
	σ_{Al}/nm	0.0	0.0	0.0	0.0
	$\sigma_{Al_2O_3}/nm$	0.0	6.3	6.1	25.7
	$d_{Al_2O_3}/nm$	1.6	1.6	1.6	1.6

Figure 8 shows the thus obtained optical constants for all samples. From the figures, we recognize the typical dispersion of metal optical constants in the spectral region from the near infrared to the UV. The comparison with reference data from [12] (black squares) confirms the physical relevance of the obtained refractive index and extinction coefficient data.

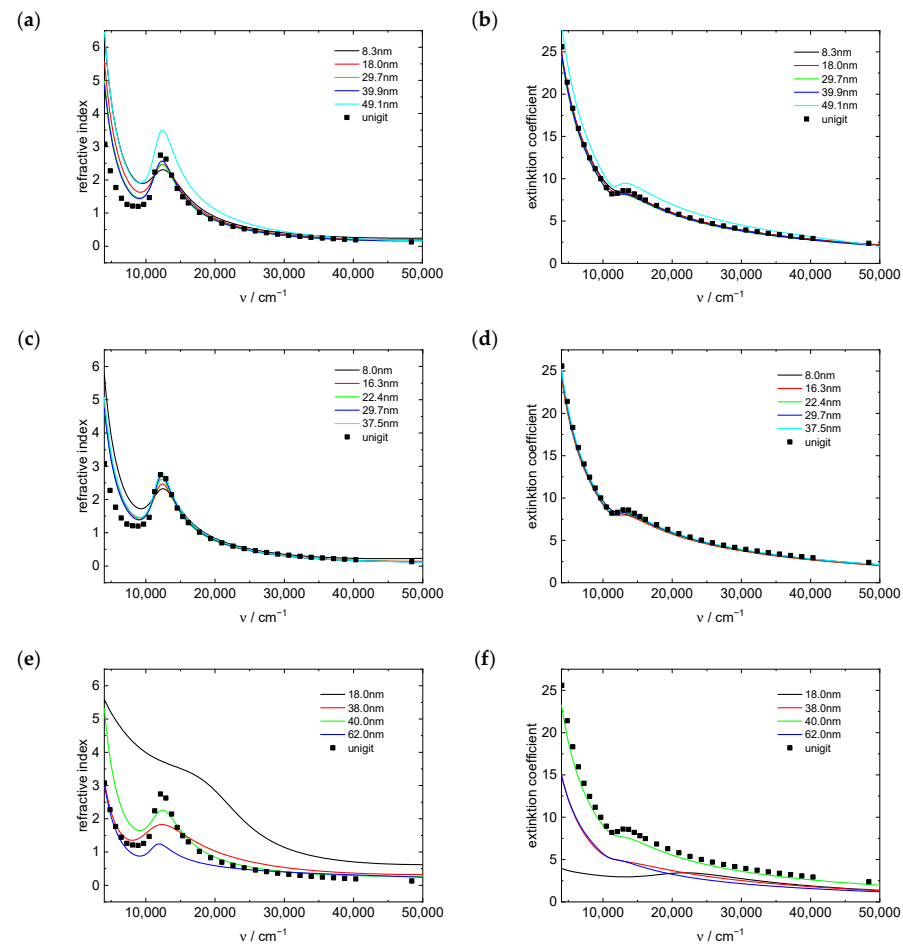


Figure 8. Optical constants for sputtering series 1 (a,b), evaporation series 2 (c,d) and assisted evaporation series 3 (e,f); left: n; right: k.

Note that there is a rather large data scatter in optical constants as obtained from the series 3 samples. For these samples, the fit was of only mere quality, while the best fit corresponded to the 40 nm sample. For this sample, best coincidence of the obtained optical constants with the reference data is evident. Obviously, the deposition process was unstable, resulting in a bad repeatability in layer properties. The 40 nm sample data obviously correspond to a closed aluminum film, while the 18 nm film results are far from being relevant for a closed aluminum film. The other two samples might be tackled as aluminum films with a rather bad optical quality.

From these results we may conclude that the majority of the investigated aluminum samples could be well fitted with the dispersion approach formulated in Equation (1). We obtain a total of 11 dispersion parameters for each layer that reproduces the optical behavior in the wavelength range between 200 and 2500 nm, corresponding to a wavenumber range between 4000 and 50,000 cm^{-1} .

5. Discussion

As a first point, let us remark the excellent correspondence between target thicknesses and measured thicknesses as verified in Figure 3. We particularly notify the agreement between the XRR thickness and the thickness obtained from transmittance and reflectance within the sum-rule approach. As it has been argued for the first time in [41], the latter thus provides an efficient tool for ultrathin metal layer thickness determination by optical means, as long as a transmittance signal different from zero may be detected (compare also [18] in this regard, where the method is applied to the thickness determination of aluminum films, although in a narrower spectral range).

Moreover, the Drude damping parameter shows the expected thickness dependence for the ultrathin layers (compare Equation (8)). This is visualized in Figure 9 for all samples except the thinnest layer from series 3. Moreover, data for copper and gold are included as reference. In our aluminum films, the mean free path effects seem to saturate at a thickness around 30–40 nm, which agrees with the characteristic thickness reported by Du [20] and is in best correspondence with Gall's theoretical value $2v_F\tau_{b0} = 37.8$ nm (compare [32]). Note that in copper and gold, that saturation thickness is somewhat larger, as expected from theoretical data [32] and evident from the descent in Figure 9.

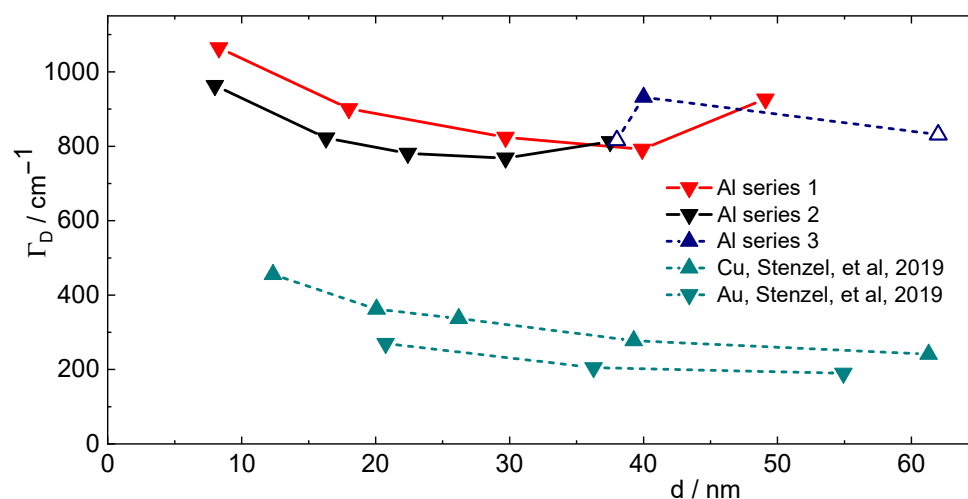


Figure 9. Dependence of the Drude damping parameter on the thickness [21].

The reason for the increase in the aluminum Drude damping parameters for a thickness larger than approximately 40 nm is unclear at the moment. Here, future work is planned to have a more detailed look at aluminum samples with a thickness of up to 100 nm. On the contrary, in closed layers with thicknesses well below 8 nm, according to Equation (8), even larger Drude damping parameters must be expected.

In fact, Equation (8) even predicts an infinitely large damping parameter when the thickness approaches zero. One should however keep in mind that further reduction of the thickness would at the same time make the assumption on a three-dimensional movement of the free electrons invalid. The confinement of the electrons motion along the layer axis in ultrathin layers would then result in quantization effects, such that one would have to apply the theory of a two-dimensional electron gas with confinement along the third coordinate axis [43].

When comparing the optical properties of aluminum layers prepared by different techniques, we will restrict on series 1 (sputtering) and series 2 (evaporation), because of the bad repeatability of the series 3 (assisted evaporation) samples. Let us choose two samples of comparable thickness (here 29.7 nm) and compare their reflectance. This is shown in Figure 10.

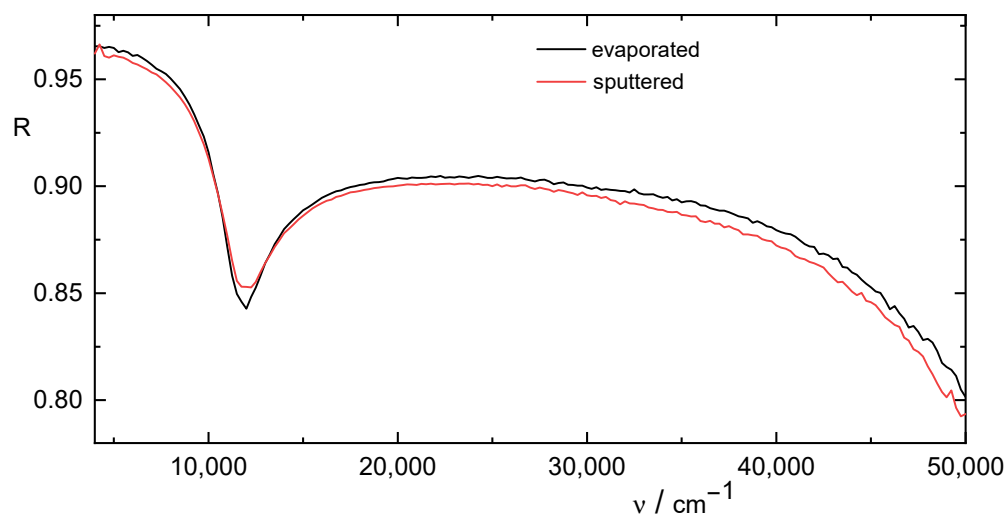


Figure 10. Near normal incidence reflection spectra of a sputtered and an evaporated sample. The thickness of both samples turned out to be 29.7 nm.

In Figure 10, we recognize the typical spectral feature in the NIR aluminum reflectance located at around $12,000 \text{ cm}^{-1}$ (830 nm). In our study, it is described in terms of the β_{do} model, and it seems to be somewhat broader for the sputtered sample. Indeed, when looking into the dispersion data presented in Tables 5 and 6, we recognize that the sputtered sample has a somewhat larger Γ -value (Table 8). Moreover, at smallest wavenumbers, the reflectance of the evaporated film is somewhat larger than that of the sputtered one. This correlates with corresponding differences in the Drude damping parameter Γ_D . Finally, at largest wavenumbers, the evaporated layer again has a somewhat larger reflectance. Empirically, this correlates with a somewhat larger plasma frequency of the evaporated layer compared to the sputtered one. This way we obtain some “rules of thumb” that establish a correspondence between the sample quality and selected dispersion parameters (Table 8).

Table 8. Comparison of selected dispersion parameters of the sputtered and evaporated aluminum films with 29.7 nm thickness.

Preparation Method	Γ/cm^{-1}	Γ_D/cm^{-1}	ν_p/cm^{-1}
“rule of thumb”	A large Γ broadens the NIR spectral feature	A small Γ_D enhances IR reflectance	A large ν_p enhances UV reflectance
sputtering	1727.6	823.9	105,132
evaporation	1546.6	767.5	106,440

All these “rules of thumb” may be verified in terms of reflectance calculation of a metal surface when modelling the optical constants in terms of Equations (1)–(4).

Note further that for the vacuum ultraviolet (VUV) reflectance, we will have to consider at least two additional loss mechanisms. Thus, in the VUV, the native aluminum oxide surface layer will become strongly absorbing [3,44,45]. Recent simulations of He [46] have shown, that the corresponding average loss between the wavelength from 120 nm to 200 nm may be of the order of 20%. Moreover, because of the smaller wavelength in the VUV, the roughness of the aluminum surface has to be taken into account explicitly. At a wavelength smaller than 200 nm, the corrugated aluminum surface gives rise to an additional optical loss resulting from both absorption and scattering mechanisms. As estimated in [46], this results in an additional averaged optical loss of about 7% when the roughness is in the range as shown in Figure 6 of the present study. The detailed simulation of VUV optical losses will be the topic of a forthcoming publication where, in particular, the earlier mentioned lateral characteristics of the aluminum surface profile become crucial for understanding the spectral behavior of the measured reflectance.

This way we come to the last point in this section, concerning the roughness-values obtained from the different characterization techniques (Figure 6). Clearly, AFM detects the roughness of the outermost surface, according to Figure 2 this is the alumina–air interface. XRR gives principal access to the roughness of buried interfaces too, and therefore, Table 4 summarizes information on the roughness data of both alumina–air and aluminum–alumina interfaces. In principle, the T- and R-spectra also contain information about these interfaces, but in the course of spectra fitting, the algorithm tended to set the roughness of the aluminum–alumina interface equal to zero while adjusting a roughness of the alumina–air interface only. For that reason, Figure 6 only contains data on the roughness of the sample surface, i.e., the alumina–air interface.

This raises the question on the reason of the rather large roughness values obtained from the fit of transmittance and reflectance. The obvious reason is in the layer model used for the fit. Concerning the alumina overlayer, it is likely to have a stoichiometry slightly different from Al_2O_3 , which means that it surely gives rise VIS/UV absorption losses. On the other hand, because of a lack of knowledge on the true optical constants of the understoichiometric Al_xO_y overlayer, the latter was modelled assuming optical constants of stoichiometric alumina, which has no relevant absorption in the regarded spectral region. Therefore, in order to model close-to-surface extra optical losses, the only chance the algorithm had was to artificially enhance the surface roughness, thus reinterpreting the absorption losses to scatter losses. Therefore, as a trend, the roughness from the NIR/VIS/UV spectra fits is considerably larger than that obtained from AFM and XRR, while the latter clearly represent the more realistic values.

6. Summary and Outlook

In this study, we provided extended data on the optical properties of thin aluminum films prepared by evaporation and sputtering. Most of the spectra could be well fitted within a dispersion approach combining the classical Drude- and Oscillator models with the β_{do} model applied here for fitting the characteristic NIR spectral feature of aluminum.

In a broader context, we would like to emphasize that the proper parametrization of a dielectric function such as given in Equations (2)–(4) might be a helpful pre-requisite for implementing artificial-intelligence-based spectra evaluation procedures into the optical characterization portfolio [47]. Thus, the dispersion parameters as given in Table 8 have a clear effect on the measured reflection spectra. A properly trained neural network surely should be able to provide at least initial guesses on those parameters from the measured reflectance only, which could subsequently be used as reliable starting values in an accurate numerical spectra fit.

The present study did not explicitly consider lateral features of the aluminum surface profile when modelling the reflectance spectra of the films. Moreover, a possible absorption within the native aluminum oxide overlayer has not been taken into account. This clearly

limits the validity of our study to a wavelength larger than approximately 200 nm. A more refined treatment that allows extending our study to the VUV spectral range is in preparation and will be the topic of a forthcoming publication.

Author Contributions: Conceptualization, O.S., S.W. and S.S. (Sven Stempfhuber); methodology, S.W., O.S., A.L., P.M., S.S. (Stefan Schwinde), S.S. (Sven Stempfhuber), N.F., M.T. and T.S.; software, S.W.; validation, all authors; formal analysis, S.W., O.S., A.L., P.M., S.S. (Stefan Schwinde), S.S. (Sven Stempfhuber), N.F., M.T. and T.S.; investigation, S.W., O.S., A.L., P.M., S.S. (Stefan Schwinde), S.S. (Sven Stempfhuber), N.F., M.T. and T.S.; resources, S.W., O.S., A.L., P.M., S.S. (Stefan Schwinde), S.S. (Sven Stempfhuber), N.F., M.T. and T.S.; data curation, all authors; writing—original draft preparation, O.S.; writing—review and editing, all authors; visualization, O.S., S.W., A.L., N.F., M.T. and T.S.; supervision, O.S.; project administration, S.W.; funding acquisition, S.W., O.S. and S.S. (Sven Schröder). All authors have read and agreed to the published version of the manuscript.

Funding: The study was partially funded by Fraunhofer-Gesellschaft internal project.

Institutional Review Board Statement: Not applicable.

Informed Consent Statement: Not applicable.

Data Availability Statement: Data underlying the results presented in this paper are not publicly available at this time but may be obtained from the authors upon reasonable request.

Acknowledgments: The authors gratefully acknowledge Michael Scheler (IOF) for the deposition of the sputtered coatings.

Conflicts of Interest: The authors declare no conflict of interest.

References

1. Hass, G. Filmed surfaces for reflecting optics. *J. Opt. Soc. Am.* **1955**, *45*, 945–952. [CrossRef]
2. Gutiérrez-Luna, N.; Perea-Abarca, B.; Espinosa-Yáñez, L.; Honrado-Benítez, C.; de Lis, T.; Rodríguez-de Marcos, L.V.; Aznárez, J.A.; Larruquert, J.I. Temperature Dependence of AlF₃ Protection on Far-UV Al Mirrors. *Coatings* **2019**, *9*, 428. [CrossRef]
3. Wilbrandt, S.; Stenzel, O.; Nakamura, H.; Wulff-Molder, D.; Duparré, A.; Kaiser, N. Protected and enhanced aluminum mirrors for the VUV. *Appl. Opt.* **2014**, *53*, A125–A130. [CrossRef]
4. Gläser, H.J. *Dünnschichttechnologie auf Flachglas*; Hofmann-Verlag GmbH & Co., KG: Schorndorf, Germany, 1999; pp. 164–248.
5. Willey, R.R. *Practical Production of Optical Thin Films*, 4th ed.; Lulu.com: Morrisville, NC, USA, 2017.
6. Uhlig, H.; Stöckl, W.; Scheler, M. Electron Beam Vaporizer, Used for Vaporizing Aluminum, Comprises High Temperature Container Made of Electrically-Conducting Ceramic for Receiving Vaporized Material Inserted into Liquid-Cooled Crucible. German Patent Application DE 199 55 428 A 1, 18 November 1999.
7. Ehrenreich, H.; Philipp, H.R.; Segall, B. Optical Properties of Aluminum. *Phys. Rev.* **1963**, *132*, 1918–1928. [CrossRef]
8. Ordal, M.A.; Long, L.L.; Bell, R.J.; Bell, R.R.; Alexander, R.W.; Ward, C.A. Optical properties of the metals Al, Co, Cu, Au, Fe, Pb, Ni, Pd, Pt, Ag, Ti, and W in the infrared and far infrared. *Appl. Opt.* **1983**, *22*, 1099–1119. [CrossRef] [PubMed]
9. Rakić, A.D. Algorithm for the determination of intrinsic optical constants of metal films: Application to aluminum. *Appl. Opt.* **1995**, *34*, 4755–4767. [CrossRef]
10. Schmitt, P.; Stempfhuber, S.; Felde, N.; Szeghalmi, A.V.; Kaiser, N.; Tünnermann, A.; Schwinde, S. Influence of seed layers on the reflectance of sputtered aluminum thin films. *Opt. Express* **2021**, *29*, 19472–19485. [CrossRef]
11. Stempfhuber, S.; Felde, N.; Schwinde, S.; Trost, M.; Schenk, P.; Schröder, S.; Tünnermann, A. Influence of seed layers on optical properties of aluminum in the UV range. *Opt. Express* **2020**, *28*, 20324–20333. [CrossRef]
12. Unigit Grating Solver Software. Available online: <https://www.unigit.net> (accessed on 24 August 2022).
13. Macleod, H.A. *Thin-Film Optical Filters*, 4th ed.; CRC Press: Boca Raton, FL, USA, 2010.
14. Willey, R.R.; Goldstein, F.T. Designing with Very Thin Optical Films. In Proceedings of the OSA Technical Digest of Optical Interference Coatings (OIC) Conference, Santa Ana Pueblo, NM, USA, 2–7 June 2019. Paper TC.5. [CrossRef]
15. Rumsby, P.; Baloukas, B.; Zabeida, O.; Martinu, L. Continuous ultra-thin silver films obtained by a two-step method for improved control of the optical and microstructural characteristics. In Proceedings of the OSA Technical Digest of Optical Interference Coatings (OIC) Conference, Vancouver, BC, Canada, 19–24 June 2022.
16. Moreau, A.; Shurvinton, R.; Morati, N.; Lemarchand, F.; Eles, B.; Destouches, N.; Lumeau, J. Development and applications of ultra-thin metallic films fabricated by Physical Vapor Deposition. In Proceedings of the OSA Technical Digest of Optical Interference Coatings (OIC) Conference, Vancouver, BC, Canada, 19–24 June 2022.
17. Sytchkova, A.; Belosludtsev, A.; Volosevičienė, L.; Juškėnas, R.; Simniškis, R. Optical, structural and electrical properties of sputtered ultrathin chromium films. *Opt. Mater.* **2021**, *121*, 111530. [CrossRef]

18. Gäbler, J.; Stenzel, O.; Wilbrandt, S.; Kaiser, N. Optische in-situ Prozessverfolgung und -steuerung des Aufdampfens optischer Beschichtungen durch gleichzeitige Messungen des Transmissions- und Reflexionsvermögens der wachsenden Schicht. *Vak. Forsch. Und Prax.* **2013**, *25*, 22–26. [[CrossRef](#)]
19. Stenzel, O. *Optical Coatings: Material Aspects in Theory and Practice*; Springer: Berlin/Heidelberg, Germany, 2014; pp. 307–311.
20. Du, H.; Xiao, J.Q.; Zou, Y.S.; Wang, T.G.; Gong, J.; Sun, C.; Wen, L.S. Optical properties of ultrathin aluminum films deposited by magnetron sputtering in visible band. *Opt. Mater.* **2006**, *28*, 944–949. [[CrossRef](#)]
21. Stenzel, O.; Wilbrandt, S.; Stempfhuber, S.; Gäbler, D.; Wolleb, S.J. Spectrophotometric Characterization of Thin Copper and Gold Films Prepared by Electron Beam Evaporation: Thickness Dependence of the Drude Damping Parameter. *Coatings* **2019**, *9*, 181. [[CrossRef](#)]
22. Kreibig, U. Optics of Nanosized metals. In *Handbook of Optical Properties II: Optics of Small Particles, Interfaces, and Surfaces*; Hummel, R.E., Wißmann, P., Eds.; CRC Press Inc.: Boca Raton, FL, USA, 1997; pp. 145–190.
23. Held, M.; Stenzel, O.; Wilbrandt, S.; Kaiser, N.; Tünnermann, A. Manufacture and characterization of optical coatings with incorporated copper island films. *Appl. Opt.* **2012**, *51*, 4436–4447. [[CrossRef](#)]
24. Amotchkina, T.V.; Janicki, V.; Sancho-Parramon, J.; Tikhonravov, A.V.; Trubetskov, M.K.; Zorc, H. General approach to reliable characterization of thin metal films. *Appl. Opt.* **2011**, *50*, 1453–1464. [[CrossRef](#)]
25. Belosludtsev, A.; Sytchkova, A.; Kyžasa, N.; Bitinaitis, I.; Simniškis, R.; Drazdys, R. Ultrathin sputtered silver films protected by ALD alumina: Comparison of in-situ investigation with ex-situ resistance and ellipsometric measurements. *Vacuum* **2022**, *195*, 110669. [[CrossRef](#)]
26. Ordal, M.A.; Bell, R.J.; Alexander, R.W.; Long, L.L.; Querry, M.R. Optical properties of fourteen metals in the infrared and far infrared: Al, Co, Cu, Au, Fe, Pb, Mo, Ni, Pd, Pt, Ag, Ti, V, and W. *Appl. Opt.* **1985**, *24*, 4493–4499. [[CrossRef](#)] [[PubMed](#)]
27. Born, M.; Wolf, E. *Principles of Optics*; Pergamon Press: Oxford, UK, 1968.
28. Dobrowolski, J.H.; Ho, F.C.; Waldorf, A. Determination of optical constants of thin film coating materials based on inverse synthesis. *Appl. Opt.* **1983**, *22*, 3191–3200. [[CrossRef](#)]
29. Wilbrandt, S.; Stenzel, O. Empirical extension to the multioscillator model: The beta-distributed oscillator model. *Appl. Opt.* **2017**, *56*, 9892–9899. [[CrossRef](#)]
30. Stenzel, O.; Wilbrandt, S. Beta-distributed oscillator model as an empirical extension to the Lorentzian oscillator model: Physical interpretation of the β_{do} model parameters. *Appl. Opt.* **2019**, *58*, 9318–9325. [[CrossRef](#)]
31. Stenzel, O. *The Physics of Thin Film Optical Spectra: An Introduction*, 2nd ed.; Springer: Cham, Switzerland, 2016; pp. 25–39.
32. Gall, D. Electron mean free path in elemental metals. *J. Appl. Phys.* **2016**, *119*, 085101. [[CrossRef](#)]
33. Orosco, J.; Coimbra, C.F.M. On a causal dispersion model for the optical properties of metals. *Appl. Opt.* **2018**, *57*, 5333–5347. [[CrossRef](#)] [[PubMed](#)]
34. Zeman, E.J.; Schatz, G.C. An accurate electromagnetic theory study of surface enhancement factors for silver, gold, copper, lithium, sodium, aluminum, gallium, indium, zinc, and cadmium. *J. Phys. Chem.* **1987**, *91*, 634–643. [[CrossRef](#)]
35. Anderson, J.C. Conduction in thin semiconductor films. *Adv. Phys.* **1970**, *79*, 311–338. [[CrossRef](#)]
36. Weißmantel, C.; Hamann, C. *Grundlagen der Festkörperphysik*; Springer: Berlin, Germany, 1979; pp. 413–416.
37. *DIN EN ISO 25178-2:2012*; Geometrical Product Specifications (GPS)—Surface Texture: Areal—Part 2: Terms, Definitions and Surface Texture Parameters. Beuth Verlag: Berlin, Germany, 2012. [[CrossRef](#)]
38. American Society of Mechanical Engineers. *Surface Texture (Surface Roughness, Waviness and Lay): ASME B46.1-2002*; ASME: New York, NY, USA, 2002.
39. Duparré, A.; Ferre-Borrull, J.; Glied, S.; Notni, G.; Steinert, J.; Bennett, J.M. Surface characterization techniques for determining the root-mean-square roughness and power spectral densities of optical components. *Appl. Opt.* **2002**, *41*, 154–171. [[CrossRef](#)] [[PubMed](#)]
40. Schröder, S.; Herffurth, T.; Trost, M.; Duparré, A. Angle- resolved scattering and reflectance of extreme-ultraviolet multilayer coatings: Measurement and analysis. *Appl. Opt.* **2010**, *49*, 1503–1512. [[CrossRef](#)]
41. Stenzel, O.; Macleod, A. Metal-dielectric composite optical coatings: Underlying physics, main models, characterization, design and application aspects. *Adv. Opt. Technol.* **2012**, *1*, 463–481. [[CrossRef](#)]
42. Tikhonravov, A.V.; Trubetskov, M.K.; Tikhonravov, A.A.; Duparré, A. Effects of interface roughness on the spectral properties of thin films and multilayers. *Appl. Opt.* **2003**, *42*, 5140–5148. [[CrossRef](#)]
43. Gross, R.; Marx, A. *Festkörperphysik*, 2nd ed.; de Gruyter: Berlin, Germany, 2014; pp. 301–303.
44. French, R.H.; Müllejans, H.; Jones, D.J. Optical properties of aluminium oxide: Determined from vacuum ultraviolet and electron energy-loss spectroscopies. *J. Am. Ceram. Soc.* **1998**, *81*, 2549–2557. [[CrossRef](#)]
45. Edmends, J.S.; Maldé, C.N.; Corrigan, S.J.B. Measurements of the far ultraviolet reflectivity of evaporated aluminium films under exposure to O₂, H₂O, CO and CO₂. *Vacuum* **1990**, *40*, 471–475. [[CrossRef](#)]
46. He, J.Y. Modelling UV and VUV Optical Losses of Rough Aluminum Films. Master’s Thesis, Friedrich Schiller University Jena, Abbe School of Photonics, Jena, Germany, 23 June 2022.
47. Wilbrandt, S.; Petrich, R.; Stenzel, O. Optical interference coating characterization using neural networks. *Proc. SPIE* **1999**, *3738*, 517–528. [[CrossRef](#)]